

## Electrodeposition of $\text{Bi}_2\text{Te}_3$ thin films onto FTO substrates from DMSO solution

M. Abellán\*, R. Schrebler and H. Gómez

Instituto de Química, Facultad de Ciencias, Pontificia Universidad Católica de Valparaíso, Av. Universidad 330, Curauma, Valparaíso, Chile.

\*E-mail: [marian.abellan@gmail.com](mailto:marian.abellan@gmail.com)

Received: 3 June 2015 / Accepted: 29 June 2015 / Published: 28 July 2015

---

We report the pulsed electrodeposition (PED) of  $\text{Bi}_2\text{Te}_3$  thin films from  $\text{TeCl}_4$  and  $\text{Bi}(\text{NO}_3)_3$  precursors dissolved in dimethylsulfoxide (DMSO) onto  $\text{SnO}_2:\text{F}$  coated glasses (FTO) and CdTe/FTO substrates. Results of a detailed set of chronoamperometric experiments allowed us to simulate the corresponding experimental  $j/t$  transients through their fitting with different possible contributions involved in the nucleation-growth mechanisms (NGMs) of the  $\text{Bi}_2\text{Te}_3$  phase. From this information it was possible to employ a set of potential/time step programs intended to select those resulting in adherent good quality thin films. AFM and SEM micrographs exhibited complete substrate coverage whereas EDX analysis gave Bi/Te ratios close to the expected stoichiometry. High-resolution X-ray diffraction analysis showed that the films were grown in the trigonal phase without the presence of other phases. From electrochemical impedance spectroscopy measurements it was possible to establish the n- type conductivity of the films which was further confirmed by photoelectrochemical experiments. Results open the possibility of using electrodeposited  $\text{Bi}_2\text{Te}_3$  thin films instead of copper as back contact in CdTe based photovoltaic solar cells.

---

**Keywords:**  $\text{Bi}_2\text{Te}_3$ , DMSO, Electrodeposition, back contact.

### 1. INTRODUCTION

Bismuth telluride ( $\text{Bi}_2\text{Te}_3$ ) is an extensively studied promising material because of its applicability in room temperature thermoelectric (TE) devices as thermoelectrical material for coolers and generators [1]. Bismuth telluride has optimal properties such as a relatively low bandgap of  $\sim 0.16$  eV, a high work function of  $\sim 5.3$  eV (close to the work function of CdTe). Both p- and n- type conductivities can be obtained by the control of the atomic percentage composition of Te with respect to the stoichiometric ones. Hence, it is an attractive candidate for stable Cu- free back contact in solar

cells based on CdTe [2]. Cu contacts present higher initial operation but its diffusion through the absorber is the main cause of the cells instability. It is also suggested that the polycrystalline nature of the films worsen this effect due to the preferential diffusion through grain boundaries.

$\text{Bi}_2\text{Te}_3$  thin films have been obtained by using different techniques such as Metal Organic Chemical Vapor deposition (MOCVD) [3], vacuum evaporation [4], Pulsed Laser Deposition (PLD) [5], sputtering [6], and electrochemical deposition [7]. Notwithstanding, the principal disadvantage of vacuum techniques is related to the large difference in the saturated vapor pressures of two compounds giving a compositional gradient along the film. Besides, a precise control of Te/Bi ratio is mandatory because it is known that changes in the stoichiometry can drastically produce changes in the semiconductor properties. Electrodeposition is a low cost method which operates at low temperatures with no vacuum demand and easily scalable to the industry. In addition, it allows to controlling composition, morphology and p- and n- type conductivities by managing electrochemical parameters such as solution composition, applied potential, pH, scan rate, temperature, etc. Most of the studies devoted to  $\text{Bi}_2\text{Te}_3$  electrodeposition are focused on the n- type synthesis onto several metals and anodized alumina oxide (AAO) substrates from acidic aqueous solution at  $\text{pH} \leq 1$  using galvanostatic methods. Magri *et al.* reported that in these conditions Te percentage in the compound decreases at higher current density [8]. On the other hand, the p- type conductivity is achieved at more negative potential than that for n- type.

In current work we have electrodeposited  $\text{Bi}_2\text{Te}_3$  employing the Pulsed Electrodeposition technique (PED) from dimethyl sulfoxide (DMSO) solution [9] containing  $\text{Bi}(\text{NO}_3)_3$  and  $\text{TeCl}_4$  as precursors. PED is more flexible than conventional galvanostatic or potentiostatic thin films electrodeposition because varying parameters such as pulse amplitude and pulse width makes possible to control both, composition and film thickness [10]. The use of organic solvents such as DMSO has advantages like high boiling points, high dielectric constants which allows to improving the Bi and Te salts solubility (as compared to water). They also offer chemical stability providing more negative potentials for boosting the formation of p-type  $\text{Bi}_2\text{Te}_3$  films. Li *et al.* have reported results of  $\text{Bi}_2\text{Te}_3$  films electrodeposition either onto porous alumina membranes and gold [11] but synthesis on FTO and CdTe has not been reported so far. After a previous voltammetric and chronoamperometric study a PED program was designed and applied to obtain films with good adherence and appropriate semiconducting properties. Morphological, structural, optical and electrical properties of the as grown films are in good agreement with those reported in the literature [12] without the need of a post thermal treatment for improving the films' quality.

## 2. EXPERIMENTAL

$\text{Bi}_2\text{Te}_3$  thin films were fabricated by PED using the methodological approach and experimental setup early reported in Ref. [8]. The films were electrodeposited from DMSO solution composed of dissolved  $\text{O}_2$  containing 0.01 M  $\text{TeCl}_4$  (> 99%, Aldrich), 0.0075 M  $\text{Bi}(\text{NO}_3)_3$  (>99.99%, Aldrich) and 1 M  $\text{NaNO}_3$  (> 99.5 %, Merck) onto  $\text{SnO}_2\text{:F}$  coated glasses (FTO, AGF Fabritech) with a sheet resistance of  $20\Omega/\text{sq}$  and CdTe/FTO. A conventional three-electrode cell was employed connected to

an Autolab PGSTAT/FRA2 potentiostat commanded by the NOVA 1.7 software. The reference electrode was a saturated Ag/AgCl 3M electrode ( $E^\circ = + 0.210$  V vs NHE), all the potentials in the text are referred to this electrode. A platinum mesh served as the counter-electrode. The FTO electrodes were rinsed and successively cleaned in an ultrasonic bath with acetone and chemically treated in fresh 1M nitric acid solution for 10 min at room temperature to improve the adherence of the films. Film electrodeposition was performed applying a pulsed E/t program following the information provided by a previous voltammetric study.  $\text{NaNO}_3$  was added as a supporting electrolyte to increase the solution conductivity. DMSO provides a wider electrochemical window for  $\text{Bi}_2\text{Te}_3$  electrodeposition from Te and Bi precursors. This expanded potential window allows for the use of more negative potentials without reduction of the solvent, thus preventing the formation of  $\text{H}_2$  bubbles. A scan rate of 0.02 V/s was used in the cyclic voltammetry experiments. Prior to the experiments the electrolytic solution was de-aerated by purging with Ar. All the experiments were performed at room temperature. Physical properties were investigated by combining morphological, structural and electrical techniques. The morphological characterization of the films was performed by Field Emission Scanning Electron Microscopy (FESEM, ZEISS Ultra-55) operating at 3KV. The composition of the films was obtained using combined energy-dispersive X-ray spectroscopy (EDX). The structural characterization was carried out by high-resolution X-ray diffraction (XRD) with a XRD Bruker D8 advance diffractometer in  $\theta$ - $2\theta$  mode with a copper cathode  $\text{CuK}\alpha$ , operating at 40 kV and 40 mA. The diffraction pattern was scanned between ( $2\theta$ )  $20^\circ$  and  $53^\circ$  in steps of  $0.02^\circ$  at speed of  $2^\circ/\text{min}$ . Raman measurements have been excited with the 532 nm laser line using a LabRAM HR UV system with a Peltier-cooled CCD and resolution better than  $2\text{ cm}^{-1}$ . The Mott-Schottky analysis was carried out to study the electronic properties using a potentiostat/ galvanostat (Zahner model IM6e) equipped with Thales software. A 0.05 mM  $\text{Na}_2\text{B}_4\text{O}_7$  pH= 9.2 aqueous solution without stirring and inert atmosphere was used for this purpose. Electrochemical impedance spectroscopy (EIS) measurements were recorded in darkness at 10 KHz in the potential range - 0.5 to 0.1 V for CdTe and -0.8 to 0 V for  $\text{Bi}_2\text{Te}_3$ . A Faraday cage was used for reducing possible errors due to interferences at high frequencies, whereas a Pt tip connected to the reference electrode through a  $14\mu\text{F}$  capacitor was employed for minimizing noise interferences. Photoelectrochemical studies were performed using the same electrolytic solution and set up as EIS measurements.

### 3. RESULTS AND DISCUSSION

#### 3.1. Voltammetric study ( $\text{Bi}_2\text{Te}_3$ /FTO)

The first cycle of the voltammetric response for each precursor and their mixtures is shown in figure 1(a)-(c).

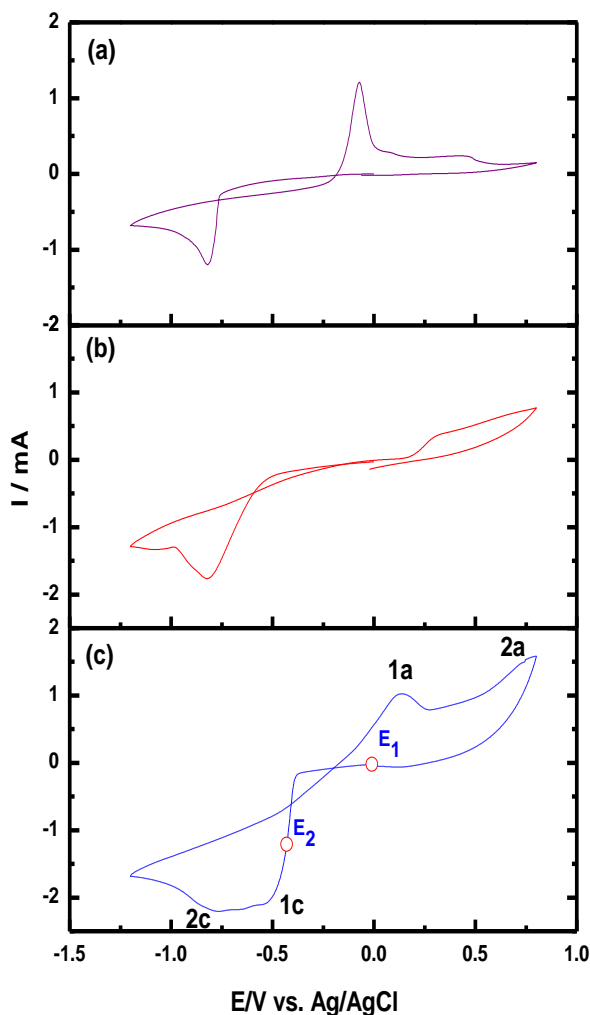
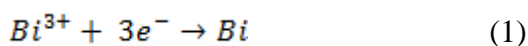
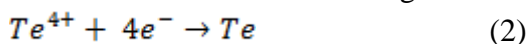


**Figure 1.** Cyclic voltammograms for DMSO solutions of: (a) 0.0075 M Bi (NO<sub>3</sub>)<sub>3</sub>, (b) 0.01 M TeCl<sub>4</sub> and (c) 0.01 M TeCl<sub>4</sub> + 0.0075 M Bi (NO<sub>3</sub>)<sub>3</sub> + 1M Na NO<sub>3</sub> (pH 3) in DMSO. Scan rate: 0.02 V·s<sup>-1</sup>.

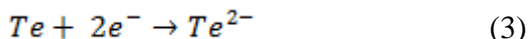
The voltammetric response for Bi<sup>3+</sup> dissolved in DMSO is presented in figure 1(a). The scan towards negative potential reveals the starting of the reduction at - 0.7 V, followed by a current peak at - 0.8 V associated to the theoretical value of a 3- electron reduction process [13], as follows:



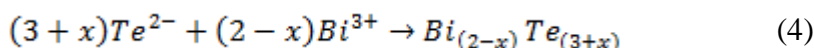
On the reverse scan, a nucleation loop is observed followed by the stripping of bismuth characterized by an anodic peak with a maximum at *ca.* - 0.07 V. Figure 1(b) shows the cyclic voltammetric scan for Te<sup>4+</sup> in DMSO. The reduction reaction begins at - 0.49 V, associated to Te<sup>4+</sup> reduction to elemental tellurium through a four electron process:



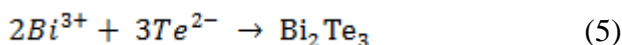
Extending the scan towards more negative potentials reveals a peak at - 0.82 V, which is associated to Te reduction in DMSO according to reaction:



The tellurium stripping is observed in the reverse scan characterized by a weak peak at 0.30 V. When bismuth and tellurium precursors are presents in solutions (figure 1(c)) the voltammetric response undergoes some changes. During the negative potential scan  $\text{Te}^{4+}$  ions adsorbed at the electrode surface are reduced to  $\text{Te}^{2-}$  at approximately - 0.35 V. Then,  $\text{Bi}^{3+}$  reacts with  $\text{Te}^{2-}$  to form a tellurium rich  $\text{Bi}_2\text{Te}_3$  phase according to [7]:



Following the cathodic scan another reduction peak (2c) is observed at - 0.84 V associated to diffusion controlled formation of  $\text{Te}^{2-}$  from  $\text{Te}^{4+}$  to form the compound through the precipitation reaction,



In the anodic scan, two broad oxidation peaks are observed. The first one (1a) at 0.13 V corresponds to the deposited bismuth telluride stripping and the second (2a) attributed to Te oxidation.

### 3.2. Nucleation and growth mechanism analysis

A set of  $E/t$  perturbation programs selected from the voltammetric results were employed in order to study the N.G.Ms of  $\text{Bi}_2\text{Te}_3$ . Figure 2 shows the respective  $j/t$  transient responses recorded between - 0.350 V and - 0.561 V where a homogeneous and adherent film is formed.

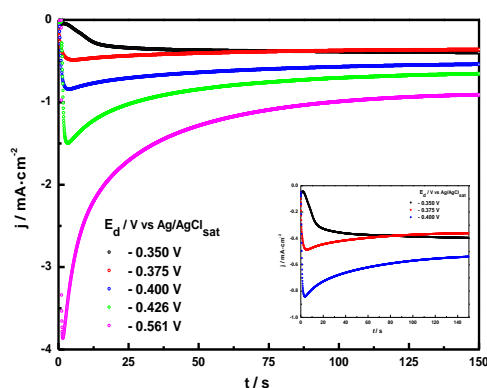


**Figure 2.** Experimental  $j/t$  transients recorded on FTO using 0.01 M  $\text{TeCl}_4$  + 0.0075 M  $\text{Bi}(\text{NO}_3)_3$  + 1M  $\text{Na NO}_3$  (pH ~ 3) as deposition bath. The inset presents the  $j/t$  experimental transients selected and fitted for the study.

These transients exhibit an induction time for the nuclei formation which decreases as the applied potential is more negative. For  $E_d = -0.350$  V the nucleation phenomenon is slow, it can be observed at around  $t < 2.5$  s. After the induction time, the current density decreases until attaining an approximately constant value. At more negative potentials values, the current achieves a maximum which is associated to nuclei coalescence. Further, the current density decreases towards a constant value indicating the contribution of a diffusion process. A detailed study of each  $j/t$  transient was performed at different potentials following the theoretical NMGs model reported by Bewick *et al.* [14]. The fitting of the transients was made including 2D and 3D nucleation processes according to the following general relationship:

$$j(t) = j_{(IN-2D)_{ct}} + j_{(PN-3D)_{ct}} + j_{(IN-3D)_{dif}} \quad (6)$$

Where:  $j_{(IN-2D)_{ct}}$  is the contribution corresponding to an instantaneous nucleation process under charge- transfer control;  $j_{(PN-3D)_{ct}}$  is a 3D progressive nucleation process under charge- transfer control, and  $j_{(IN-3D)_{dif}}$  corresponds to a 3D instantaneous nucleation mechanism controlled by diffusion. Each  $j/t$  transient can be fitted by equation (6) as follows:

$$j(t) = P_1 \cdot t \cdot e^{-P_2 t^2} + P_3 \cdot (1 - e^{-P_4 t^3}) + \frac{P_5}{t^{\frac{1}{2}}} \cdot (1 - e^{-P_6 t}) \quad (7)$$

The  $P_i$  parameters obtained from this fitted equation and its physical meaning, are shown in Table I.

**Table I.** Kinetic Parameters obtained by the Nonlinear Fitting for  $j/t$  transients and nucleation and growth proposed mechanisms.

$E_d$ /V	$P_1 = \frac{2\pi nFMh_1 Nk}{\rho}$ (As <sup>-1</sup> )	$P_2 = \frac{\pi M^2 N_{01} k_1^2}{\rho^2}$ (s <sup>-2</sup> )	$P_3 = \pi nFk_3$ (A)	$P_4 = \frac{\pi M^2 k_3^2 A_3 N_{03}}{3\rho^2}$ (s <sup>-3</sup> )	$P_5 = \frac{anFD^{\frac{1}{2}} c^\infty}{\pi^{\frac{1}{2}}}$ (As <sup>1/2</sup> )	$P_6 = -N_0 \pi kD$ (s <sup>-2</sup> )
<b>-0.350</b>	0.00002	0.00112	0.00038	0.00001		
<b>-0.375</b>	0.00025	0.16552	0.00032	0.02611	0.00062	0.16002
<b>-0.400</b>	0.00060	0.23446			0.00059	0.22762

$E_d$ : Potential step value;  $n \cdot F$ : molar mass charge transferred during the electrodeposition (A · s · mol<sup>-1</sup>);  $h_1$ : height of the bi-dimensional nuclei (cm);  $N_0, N_{01}$  and  $N_{03}$ : number of active sites under the experimental condition (cm<sup>-2</sup>);  $K, K_1$  and  $K_3$ : growth rate constant of one single nucleus (mol · cm<sup>-2</sup> · s<sup>-1</sup>);  $A_3$ : steady-state nucleation rate constant (cm<sup>-2</sup> · s<sup>-1</sup>);  $a$ : electrode area (cm<sup>2</sup>);  $M$ : molar mass (g · mol<sup>-1</sup>);  $\rho$ : density (g · cm<sup>-3</sup>);  $C^\infty$ : concentration in bulk solutions (mol · cm<sup>-3</sup>);  $D$ : diffusion coefficient (cm<sup>2</sup> · s<sup>-1</sup>);  $A_3$ : three dimensional constant rate (cm · s<sup>-1</sup>). Where  $K = \frac{4}{3} (8\pi c^\infty M)^{1/2}$ .

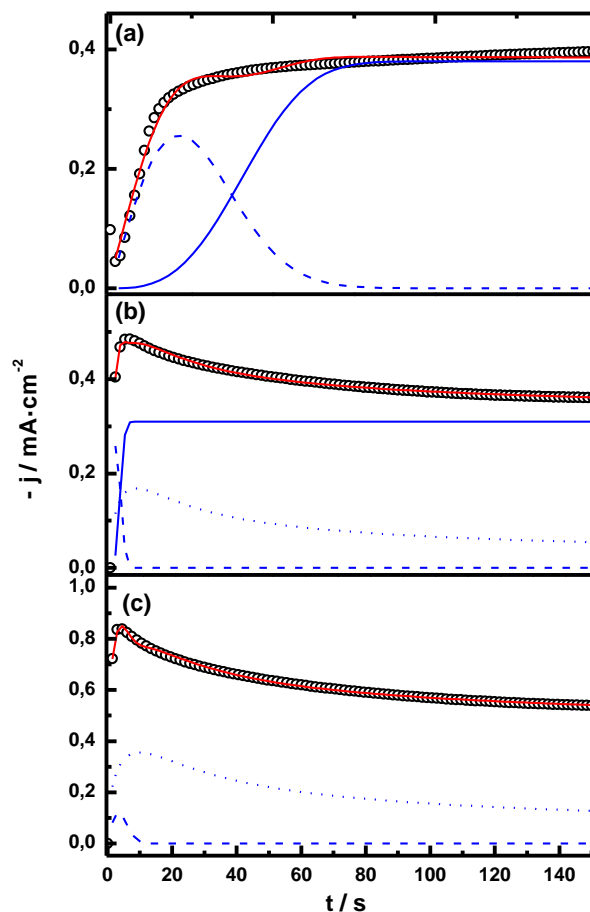


**Figure 3.** Experimental (o) and fitted (red line curve)  $j/t$  transients at (a)  $E_d = -0.350$  V, (b)  $E_d = -0.375$  V and, (c)  $E_d = -0.400$  V during the electrodeposition of  $\text{Bi}_2\text{Te}_3/\text{FTO}$ . The individual contributions of the three mechanisms of nucleation and growth calculated from the parameters of Table I are also included:  $(\text{IN-2D})_{\text{ct}}$  (---),  $(\text{PN-3D})_{\text{ct}}$  (—), and  $(\text{IN-3D})_{\text{dif}}$  (···).

The data were fitted with equation (7) considering the individual contributions of the three MNGs through the  $P_1$  parameter of Table I. Figure 3 shows the experimental and fitted curves at the selected potentials. In the case of electrodeposition at  $-0.350$  V (figure 3(a)), the deconvolution of the total density current involves only two contributions. At short times, the first one is associated to a 2D instantaneous nucleation controlled by charge transfer,  $(\text{IN-2D})_{\text{ct}}$  whereas at longer times the second contribution corresponds to a 3D progressive nucleation also controlled by charge transfer,  $(\text{PN-3D})_{\text{ct}}$ . Besides, no contributions related to a 3D instantaneous nucleation mechanism controlled by diffusion is observed at this potential. At more negative potentials (see figure 3 (b) y 3 (c)), the  $(\text{IN-2D})_{\text{ct}}$  contribution appears at shorter times than at  $-0.350$  V, however at longer times there is a new contribution which is controlled by a diffusion process. Note that for  $E_d = -0.400$  V the simulation fits very well along the whole length of the time interval considered. Besides, the fact that at short time almost immediately appears a  $(\text{IN-3D})_{\text{dif}}$  contribution seems to indicate that the 3D nuclei are generated independently of the 2D nuclei.

Regarding the kinetic parameters shown in Table I, it is possible to observe that  $P_1$ ,  $P_2$ ,  $P_4$  and,  $P_6$  values increase as the potential is more negative a behavior that can be attributed to an increasing in the nucleation rate. Furthermore,  $P_3$  and  $P_5$  parameters remain without changes given they are independent of  $E_d$ .

### 3.3. $\text{Bi}_2\text{Te}_3$ electrodeposition

Taking account the  $\text{Bi}_2\text{Te}_3$  MNGs study, a set of two steps  $E/t$  perturbation programs were selected (see figure 4).

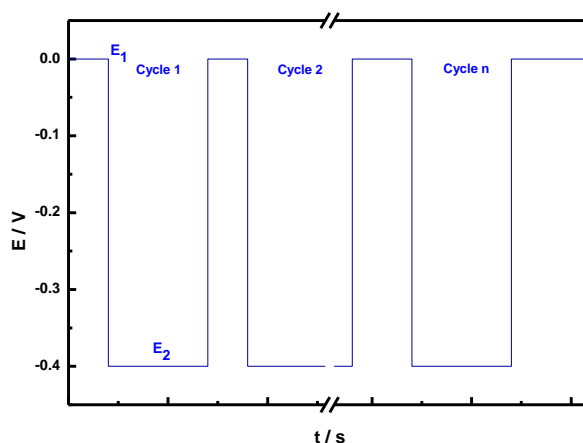


**Figure 4.**  $E/t$  program selected for  $\text{Bi}_2\text{Te}_3$  PED. Step 1:  $E_1 = 0 \text{ V}$ ;  $\tau_1 = 2\text{s}$ , no net electrochemical reduction processes take place. Step2:  $-0.400 \text{ V} \leq E_2 \leq -0.350 \text{ V}$   $\tau_2 = 5\text{s}$ ,  $\text{Bi}_2\text{Te}_3$  deposition takes place through reaction described by equation (5).

It is expected that under these conditions a 2D layer by layer growth be the process that controls the deposition resulting in homogenous films. Twelve cycles ( $\tau_T = 84\text{s}$ ) were applied to obtain films with the required thickness. To promote the 2D instantaneous nucleation the deposition times were restricted to 5s.

### 3.4. Films Characterization

#### 3.4.1. Morphological characterization

The morphological characterization of the films was made by SEM and AFM analysis. Similar morphologies were obtained for the films electrodeposited with the different potential/time programs studied. For  $E_d = -0.400 \text{ V}$  SEM images 5 (a) and (b) exhibit uniform granular morphology with an average grain size  $< 100 \text{ nm}$  which agrees with XRD results (vide infra). The surface consists in many islands compactly packed which is a typical feature of the PED technique [12]. The cross section (figure 5 (b)) images reveal a good adhesion to the substrate with no evidence of cracks through the films. The EDX measurements presented a Bi/Te atomic ratio of around 38/62 %.

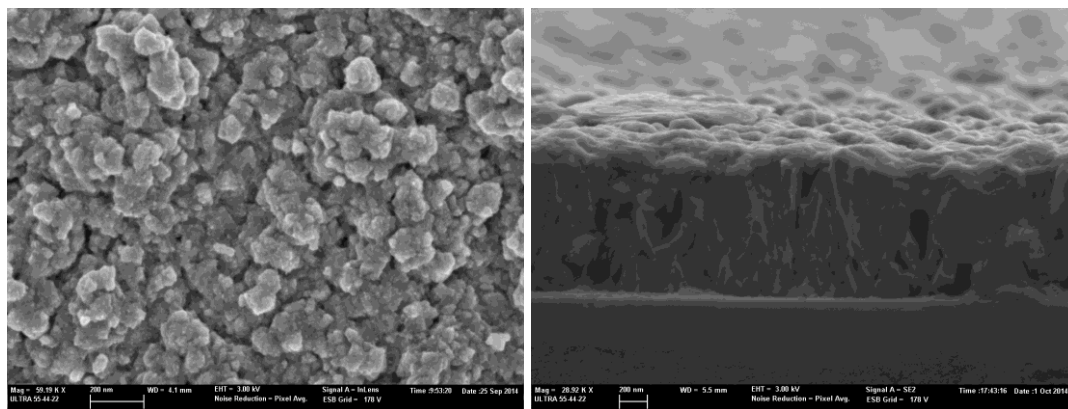


**Figure 5.** (a) Surface morphology and, (b) cross-sectional SEM images for  $\text{Bi}_2\text{Te}_3/\text{FTO}$  thin film.

AFM images show a smooth aspect with a regular microstructure in agreement with SEM micrographs. Homogeneous deposition and roughness of about  $\text{RMS} = 94 \text{ nm}$  were determinate.

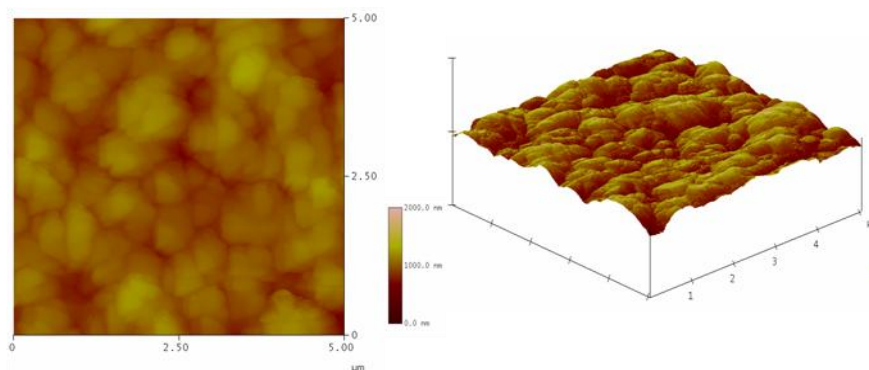


**Figure 6.** AFM images of  $\text{Bi}_2\text{Te}_3$  thin films onto FTO: (a) 2D and (b) 3D morphologies.

### 3.4.2. Structural characterization

The crystal structure of two films deposited by PED on different substrates (FTO and  $\text{CdTe}/\text{FTO}$ ) was studied by XRD in the parallel geometry. In both cases, four diffraction peaks can be observed in XRD patterns at  $27.83^\circ$ ,  $38.02^\circ$ ,  $40.91^\circ$  and  $50.07^\circ$  which are related to the (1 0 1), (0 1 5), (1 0 10), (1 1 0) and (2 0 5) reflections of trigonal  $\text{Bi}_2\text{Te}_3$  phase, (JCPDS, 15-0863) [15], respectively. Thus, these results show that the samples are polycrystalline with a preferential orientation along the (0 1 5) direction. In the case of  $\text{Bi}_2\text{Te}_3/\text{CdTe}/\text{FTO}$  the peaks located at  $23.03^\circ$ ,  $43.33^\circ$  and  $46.31^\circ$  belong to (1 0 0), (1 0 3) and (2 0 0) reflection of the hexagonal  $\text{CdTe}$  phase, (JCPDS, 19-0193) [16]. No other crystalline phases are observed, confirming the purity of the samples. Comparing the  $2\theta$  position of the (0 1 5) peak with that reported in database [15], it is observed that in both cases the  $2\theta$  positions is shifted to lower values indicating that the films present a tensile stress. Furthermore, the peak intensities of the films grown onto  $\text{CdTe}/\text{FTO}$  are greater than onto FTO which is due to the different lattice mismatch between the two substrates ( $\text{CdTe}/\text{FTO}$ :  $\Delta a/a \sim 3.7\%$ ; FTO:

$\Delta a/a \sim 32\%$ ). To assess the crystalline quality, the FWHM (Full Width at Half Maximum) for the preferential orientation was also calculated, the values obtained were  $0.8^\circ$  for  $\text{Bi}_2\text{Te}_3/\text{FTO}$  and  $0.6^\circ$  for  $\text{Bi}_2\text{Te}_3/\text{CdTe}/\text{FTO}$ , indicating that the latter film has better crystalline quality and slightly grain size. Employing the Scherrer equation for the (0 1 5) preferential orientation crystalline sizes of 40 and 42 nm were respectively calculated.

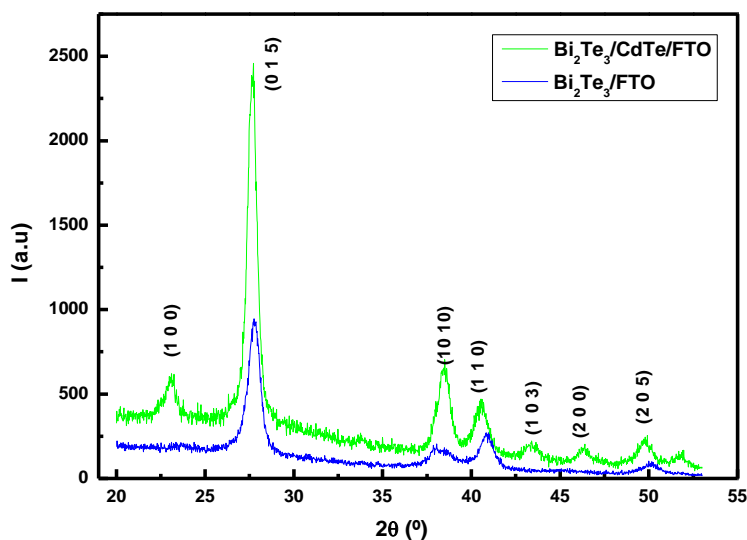


Figure 7. XRD pattern of (a)  $\text{Bi}_2\text{Te}_3/\text{FTO}$  and (b)  $\text{Bi}_2\text{Te}_3/\text{CdTe}/\text{FTO}$  deposited by PED technique.

Table II. Harris texture coefficients and standard deviations of  $\text{Bi}_2\text{Te}_3/\text{FTO}$  and  $\text{Bi}_2\text{Te}_3/\text{CdTe}/\text{FTO}$  films deposited by PED.

Film	Peak (h k l)	$I_{hkl}$	$I_{JCPDS}$	$TC_{(hkl)}$	$\sigma$
$\text{Bi}_2\text{Te}_3/\text{FTO}$	(0 1 5)	929.167	100	1.2065	0.1192
	(1 0 10)	196.667	25	0.6450	0.2050
	(1 1 0)	223.339	25	1.1485	0.0857
<b><math>\text{Bi}_2\text{Te}_3/\text{CdTe}/\text{FTO}</math></b>					
CdTe	(1 0 0)	96.911	90	1.0470	0.0269
	(1 0 3)	42.2849	42.717	0.9622	0.0218
	(2 0 0)	46.315	45.425	0.9911	0.0051
$\text{Bi}_2\text{Te}_3$	(0 1 5)	961.756	100	1.2637	0.1522
	(1 0 10)	218.507	25	1.1484	0.0857
	(1 1 0)	120.096	25	0.6312	0.2129

$TC_{(hkl)}$ : Texture Coefficient,  $I_{hkl}$ : Intensity of the (hkl) peak observed in the experiment,  $I_{JCPDS}$ : Intensity of the (hkl) peak found in the literature [15,16],  $\sigma$ : the associated standard deviation.

The values of texture coefficients and their standard deviations were also calculated. Only the more intense peaks were considered as shown in table II. In both cases the texture coefficient is higher

than 1 meaning that the peak is associated to a preferential plane growing, confirming thus that the films is strongly oriented along the (0 1 5) direction.

Raman spectra of the as-grown  $\text{Bi}_2\text{Te}_3$  thin film recorded in the range 20 - 54  $\text{cm}^{-1}$  and it is depicted in figure 8 (a). The spectrum was analyzed to verify the  $\text{Bi}_2\text{Te}_3$  and to look for the presence of traces of other components which could be possible by means PED.

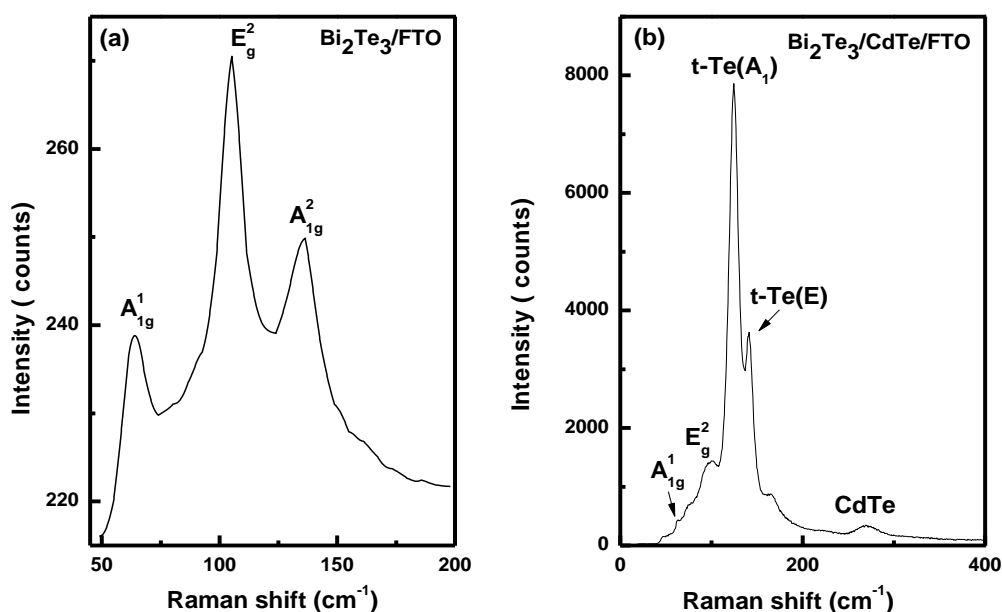


**Figure 8.** Typical Raman spectrums of (a)  $\text{Bi}_2\text{Te}_3/\text{FTO}$  and (b)  $\text{Bi}_2\text{Te}_3/\text{CdTe}/\text{FTO}$  thin films.

The Raman bands of  $\text{Bi}_2\text{Te}_3$  show the vibrational modes centered at 63.24  $\text{cm}^{-1}$ , 101.98  $\text{cm}^{-1}$  and 133.03  $\text{cm}^{-1}$  correspond to the,  $A_{1g}^1$ ,  $E_g^2$  and  $A_{1g}^2$  phonon modes respectively [17,18]. The  $A_{1g}^1$  mode indicates the stretching mode along the c-axis within the Bi-Te quintuple layers. The  $E_g^2$  is associated to an interplanar vibration mode [19]. This vibration mode corresponds to the vibration of Bi-Te quintuple layers along the c-axis which is presented in bismuth telluride films with near stoichiometric composition [20]. The  $A_{1g}^2$  mode involves the bonding forces between the bismuth and tellurium atoms. A slightly excess in Te is reflected in a widening and shift of the  $A_{1g}^2$  mode, in agreement with the EDX analysis. Likewise, the  $\text{Bi}_2\text{Te}_3/\text{CdTe}$  (see figure 8 (b)) films present the  $E_g^2$  mode associated to  $\text{Bi}_2\text{Te}_3$  and the peak associated to  $A_{1g}^2$  modes is hidden by the CdTe signal because of the higher signal intensity presented by this material. The bands centered at 124.81  $\text{cm}^{-1}$  and 141.31  $\text{cm}^{-1}$  corresponds to the  $A_1$  and E phonon modes respectively. These Raman modes are attributed to the presence of tensile stress on Te precipitates in CdTe [21]. The weak mode observed around 164.24  $\text{cm}^{-1}$  is identified with the longitudinal optic (LO) phonon mode. It must be taken into account that the film presents a dominant peak corresponding to the Te vibrational mode, which indicates a Te excess. This is due to the Cd evaporation in the surface during the laser exposition. Soares *et al.* [22] showed by Q-Raman that visible radiation leads to the formation of Te aggregates on the irradiated surface,

compromising any conclusion about Te inclusions on CdTe surface, and speculating that heating by laser light could break chemical bond producing Cd evaporation, thus leaving a Te excess at the surface.

### 3.4.3. Electrochemical characterization

The optoelectronic properties of the Bi<sub>2</sub>Te<sub>3</sub> film samples were studied employing electrochemical impedance spectroscopy measurements. The analysis of the interfacial capacitance vs potential data were analyzed from the Mott–Schottky equation written as [23]:

$$\frac{1}{C_{SC}^2} = \frac{2}{qN_D \epsilon \epsilon_0} \left( V + V_{FB} - \frac{KT}{q} \right) \quad (8)$$

where C is the differential capacitance of the space-charge region, ε<sub>0</sub>, the permittivity of vacuum, ε<sub>r</sub> the relative dielectric constant (85) [24], N<sub>D</sub> the donor carrier density for n- type semiconductor or N<sub>A</sub> the acceptor carrier density for a p- type semiconductor, V the electrode potential, and V<sub>FB</sub> the flat band potential. Figure 9(a) presents the experimental curve of the plot 1/C<sup>2</sup> vs V which shows a positive slope, confirming that the Bi<sub>2</sub>Te<sub>3</sub> layer presents the semiconductor characteristic of an n- type material. The intercept at the potential axis yields -0.65 V for the flat band potential. The apparent concentration of majority carriers (N<sub>D</sub>), calculated from the slope, is 2.856 · 10<sup>18</sup> cm<sup>-3</sup>, a value that is within those reported in the literature and also comparable to the bulk material which is around 10<sup>17</sup>-10<sup>18</sup> cm<sup>-3</sup> [25].

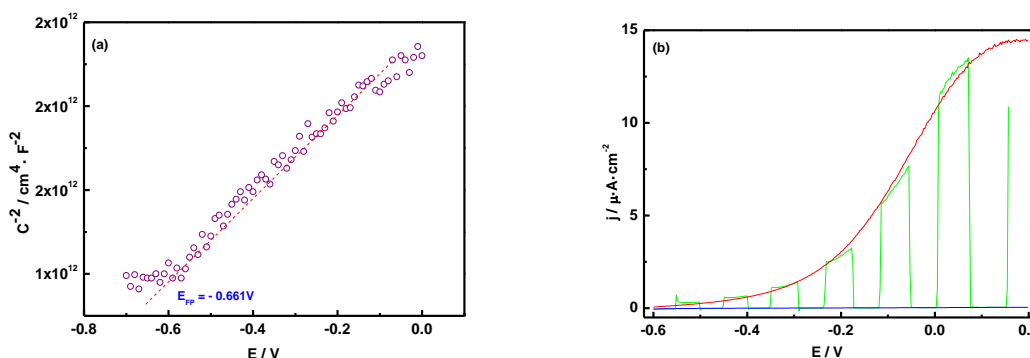


**Figure 9.** (a) Mott-Schottky plot and (b) I/E voltametric profiles carried out under conditions of darkness (----), light (----) and under chopped light (----) of Bi<sub>2</sub>Te<sub>3</sub>/FTO thin film deposited by PED in 0.05 M Na<sub>2</sub>B<sub>4</sub>O<sub>7</sub>. White illumination of 1000 W.

A semiconductor electrode should show rectifying behavior under the polarization regime corresponding to minority carrier current flow. It is expected that for a n-type material rectification be observed at potentials positive of the flatband value. Under illumination electron and holes are separated in the space charge region and further driven in opposite directions by the effect of the electric field. The n-type conductivity of Bi<sub>2</sub>Te<sub>3</sub> predicts the apparition of a positive photocurrent as result of the migration of holes towards the electrode/electrolyte interface increasing then the anodic

current.. The photocurrent was recorded using an electrolytic solution containing 0.05 M Na<sub>2</sub>B<sub>4</sub>O<sub>7</sub>, pH = 9.3. Figure 9(b) shows j/E potentiodynamic responses for the Bi<sub>2</sub>Te<sub>3</sub>/FTO electrode under different experimental conditions: in darkness, under illumination, and under chopped light conditions. As the dark current density ( $J_d$ ) is very small (about  $<10^{-8}$   $\mu\text{A}$ ) then Bi<sub>2</sub>Te<sub>3</sub> forms a blocking contact with the electrolyte. Under white light illumination, the curve exhibits an anodic photocurrent  $J_{ph}$  supporting the n- type character of the film. The photocurrent onset agrees well with the flat band potential derived from the Mott-Schottky plot ( $E_{FB} = -0.66$  V vs. SCE) according to the relation that  $J_{ph} \propto (V_{FB} - V)$  [26].

#### 4. CONCLUSIONS

PED technique has been successfully employed for the synthesis of Bi<sub>2</sub>Te<sub>3</sub> thin films onto FTO and CdTe/FTO substrates. A detailed chronoamperometric study allowed to looking for the best conditions for obtaining good quality films without the need of a post thermal treatment. SEM images revealed a good adhesion to the substrate and also high quality microstructure. EDX analysis gave a stoichiometric composition very close to the expected one. XRD analysis showed that the films grew in the trigonal phase without the presence of others phases, a consequence of using a non-aqueous solvent in the synthesis. Besides, the films showed n-type semiconducting behavior with a significant apparent carrier density concentration (around  $N_D = 2.856 \cdot 10^{18}$   $\text{cm}^{-3}$ ). Further work will be devoted to extend current results concerning to the back contact on CdTe based solar cells and evaluation of its performance.

#### ACKNOWLEDGEMENTS

This work has been supported by FONDECYT (Fondo de Desarrollo Científico y Tecnológico, Chile) through Project No. 3031451. M.A acknowledges the support received from Pontificia Universidad Católica de Valparaíso (Chile).

#### References

1. G.S. Nolas, J. Sharp, J. Goldsmid. *Thermoelectrics: Basic Principles and New Materials Developments*, Springer, New York (2001).
2. R. Tang, Z. Wang, W. Li, L. Feng, J. Zhang, L. Wu, B. Li, G. Zeng, W. Wang, *Solar Energy Materials & Solar Cells*, 121(2014) 92.
3. A. Boulouz, A. Giani, F. Pascal-Delannoy, *Journal of Crystal Growth*, 170 (1997) 817.
4. R. Tang, Z. Wang, W. Li, L. Feng, J. Zhang, L. Wu, B. Li, G. Zeng, W. Wang, *Solar Energy Materials and Solar Cells*, 121 (2014) 92 .
5. A. Bailini, F. Donati, M. Zamboni, V. Russo, M. Passoni, C.S Casari, A. Li Bassi, C.E Bottani, *Applied Surface Science*, 254 (2007) 1249.
6. D.-H. Kim, E. Byon, G.-H. Lee, S. Cho., *Thin Solid Films*, 510 (2006) 148.
7. M. S. Martín-González, A. L. Prieto, R. Gronsky, T. Sand, A. M. Stacy. *Journal of The Electrochemical Society*, 149 (2002) C546.
8. P. Magri, C. Boulanger, J.M. Lecuire, *J.Mater. Chem.*, 6(5) (1996) 773.
9. B. Marí, M. Mollar, D. Soro, R. Henríquez, R. Schrebler, H. Gómez, *Int. J. Electrochem. Sci.*, 8 (2013) 3510.

10. C. V. Manzano, A. A. Rojas, M. Decepeida, B. Abad, Y. Feliz, O. Caballero-Calero, D.A Borca-Tasciuc and M. Martin-Gonzalez. *J Solid State Electrochem.*, 17 (2013) 2071.
11. W.J. Li, W.L. Yu, C-Y Yen. *Electrochimica Acta*, 58 (2011) 510.
12. V. Richoux, S Diliberto, C. Boulanger, J.M. Lecuire. *Electrochimica Acta*, 52 (2007) 3053.
13. M. Pourbaix, Atlas of Electrochemical Equilibria in Aqueous Solutions, Pergamon Press, Oxford, New York (1966).
14. A. Bewick, M. Fleischmann, H.R. Thirsk, *Trans. Faraday Soc.*, 58 (1962) 2200.
15. Database: Joint Committee on Powder Diffraction- International Centre for Diffraction Data (JCPDS-ICDD). JCPDS, Card No 15-0863. (<http://www.icdd.com>).
16. Database: Joint Committee on Powder Diffraction- International Centre for Diffraction Data (JCPDS-ICDD). JCPDS, Card No 19-0193. (<http://www.icdd.com>).
17. O. Caballero-Calero, P. Diaz-Chao, B. Abad, C.V. Manzano, M.D. Ynsa, J.J. Romero, M.M. Rojo, M. Martin-Gonzalez, *Electrochim. Acta* ,123(2014) 117.
18. F. Song-Ke, L. Shuang-Ming, and F. Heng-Zhi, *Chin. Phys. B.*, 23 (2014) 086301.
19. L.M. Goncalves, C. Couto, P. Alpuim, A.G. Rolo, F. Völklein, J.H. Correia., *Thin Solid Films* 518 (2010) 2816
20. V. Russo, A. Bailini, M. Zamboni, M. Passoni, C. Conti, C. S. Casari, A. Li Bassi and C. E. Bottani, *J. Raman Spectrosc.*; 39(2008) 205.
21. A. S. Pine and G. Dresselhays, *Phys. Rev. B*, 4 (1971), 356.
22. M.J. Soares, J.C. Lopes, M.C. Carmo, and A. Neves, *phys. stat. sol. (c)* 1 (2004) 278.
23. Jaime González Velasco. *Fotoelectroquímica de semiconductores. Su aplicación a la conversión y almacenamiento de energía solar*, Editorial Reverté y Centro Editorial de la Universidad Autónoma de Madrid (2010).
24. W. Richter, H. Köhler, and C. R. Becker. *Phys. Stat. Sol. (b)* 6-1 (1977) 619.
25. S. Sugai, *Jpn. J. Appl. Phys.* 30 (1991) L1083.
26. N. Sato *Electrochemistry at Metal and Semiconductor Electrodes*. Elsevier, Amsterdam, (1998).

© 2015 The Authors. Published by ESG ([www.electrochemsci.org](http://www.electrochemsci.org)). This article is an open access article distributed under the terms and conditions of the Creative Commons Attribution license (<http://creativecommons.org/licenses/by/4.0/>).